arXiv:1412.3245v1 [astro-ph.SR] 10 Dec 2014

Observations and modelling of North-South asymmetries using a Flux Transport Dynamo

Juie Shetye

Armagh Observatory, College Hill, Armagh City, Northern Ireland,UK,BT61 9DG

Durgesh Tripathi

Inter-University Centre for Astronomy and Astrophysics, Post Bag - 4, Ganeshkhind, Pune 411007, India

and

Mausumi Dikpati

High Altitude Observatory, National Center for Atmospheric Research Boulder, Colorado USA 80307

ABSTRACT

The peculiar behaviour of the solar cycle 23 and its prolonged minima has been one of the most studied problems over the last few years. In the present paper, we study the asymmetries in active region magnetic flux in the northern and southern hemispheres during complete solar cycle 23 and rising phase of solar cycle 24. During the declining phase of solar cycle 23, we find that the magnetic flux in the southern hemisphere is about 10 times stronger than that in the northern hemisphere during the declining phase of the solar cycle 23 and during the rising phase of cycle 24, however, this trend reversed. The magnetic flux becomes about a factor of 4 stronger in the northern hemisphere to that of southern hemisphere. Additionally, we find that there was significant delay (about 5 months) in change of the polarity in the southern hemisphere in comparison with the northern hemisphere. These results provide us with hints of how the toroidal fluxes have contributed to the solar dynamo during the prolonged minima in the solar cycle 23 and in the rising phase of the solar cycle 24. Using a solar flux-transport dynamo model, we demonstrate that persistently stronger sunspot cycles in one hemisphere could be caused by the effect of greater inflows into active region belts in that hemisphere. Observations indicate that greater inflows are associated with stronger activity. Some other change or difference in meridional circulation between hemispheres could cause the weaker hemisphere to become the stronger one.

Subject headings: Sun: activity – Sun: photosphere – Sun: magnetic fields – Sun: sunspots

1. Introduction

Based on the observations of Sunspots on the surface of the Sun and the relatively well-organised poloidal field, which changes polarity approximately every 11 year, it has been universally accepted that the solar magnetic cycle is a dynamo process involving the transformation of the polar field into the toroidal field and subsequent conversion of the toroidal field into the poloidal field of opposite polarity over the course of approximately 11 years (see e.g. Babcock 1961, and its citations). The generation and propagation of large-scale magnetic fields via the dynamo mechanism is considered to be a two-step process. The first step involves shearing of the poloidal component of magnetic field by differential rotation, which gives rise to the azimuthally directed toroidal magnetic field. This toroidal field then gives rise to the formation of the sunspots and the active regions (henceforth ARs). The second step is the formation of the poloidal component from the toroidal component, which occurs from the magnetic flux liberated by the growth and the decay of the sunspots, with the leading polarity flux moving towards the equator and the following polarity towards the pole. In some models, movement of the following polarity fields towards poles is due to the meridional circulation, as illustrated with both the kinematic dynamo and the flux-transport dynamo models (see e.g. Wang et al. 1991; Choudhuri et al. 1995, and their citations).

The study of the solar cycle on long time scales indicates that the solar cycle is virtually symmetric between North and South hemispheres, in the sense that the average amplitudes, shapes and durations of cycles are very similar (see e.g., Goel & Choudhuri 2009). However, there are individual cycles that are known to be stronger in one hemisphere than other. For example, just after the Maunder Minimum, almost all the sunspots were observed in southern hemisphere (see e.g. Ribes & Nesme-Ribes 1993). Asymmetries between the two hemispheres have also been observed in various solar activity phenomena such as sunspot area, sunspot numbers, faculae, coronal structure, post-eruption arcades, coronal ionisation temperatures, polar field reversals as well as solar oscillations (see e.g., Chowdhury et al. 2013; Sýkora & Rybák 2010; Gao et al. 2009; Li et al. 2009; Temmer et al. 2006; Knaack et al. 2004, 2005; Tripathi et al. 2004; Ataç & Özgüç 1996; Oliver & Ballester 1994; Zolotova et al. 2010; Svalgaard & Kamide 2013, and reference therein), in addition to long term hemispheric asymmetries in solar activity in previous solar cycles (see e.g., Vizoso & Ballester 1989; Carbonell et al. 1993; Norton & Gallagher 2010).

Further, the rise and fall of solar cycle 23 has been discussed by many authors; it has

been found that the behaviour of solar cycle 23 is very peculiar for an odd-number cycle (Chowdhury et al. 2013). Cycle 23 showed a slow rise compared to other odd-numbered cycles and was found to be weak compared to other odd-numbered cycle (Li et al. 2009; Chowdhury et al. 2013). Additionally, it shows an unusual second peak during the declining phase (Li et al. 2009; Mishra & Mishra 2012). Moreover, the temporal characteristics of cycle 23, such as sunspot number and sunspot area, are similar to the Gleissberg global minimum cycles 11, 13 and 14, which occurred between 1880 and 1930, as well as solar cycle 20 (Krainev 2012). Analysis of polar field patterns indicate that polar field reversal was slower than the previous two cycles as discussed in (Dikpati et al. 2004), which could have delayed the rise of solar cycle 24. The first two years of cycle 24, with low solar activity concentrated in the South, is similar to the cycle that immediately followed the Maunder Minimum (Krainev 2012).

Our motivation for this research is to investigate solar cycle 23 and rise of solar cycle 24 by computing the AR fluxes that form the toroidal fluxes. We then concentrate on the solar cycle minimum and investigate the asymmetry in the hemispheres with the aim of addressing the issue related to the deep minimum observed in cycle 23. To support our observations, we have carried out dynamo simulations as mentioned in Belucz & Dikpati (2013). We also investigated the role of meridional circulation combined with flux asymmetry for the solar cycle 23 by discussing different cases related to the asymmetries found. The rest of the paper is organised as follows: in Section 2 we present the observations and data selection, followed by magnetic flux analysis and results in Section 3. In Section 4 we discuss dynamo simulations and relate them to our observations. In the concluding Section 5, we summarise the results and science.

2. Observations and Data

We calculate the line-of-sight (LOS) component of the magnetic field (hereafter $B_\perp$) using the magnetograms recorded by the Michelson Doppler Imager (MDI; Scherrer et al. 1995) on board the Solar Heliospheric Observatory (SoHO). MDI is an instrument used to observe signs and strength of the line-of-sight component of the photospheric magnetic field. MDI images the Sun using a 1024 × 1024 CCD camera and acquires one full-disk line-of-sight magnetic field each 96 minutes (five minutes averaged 96-min cadence), among other observing sequences, which is free from atmospheric noise. A full-disk magnetogram of the Sun has a resolution of $\sim 4''$ ($2''\times 2''$ per pixel) and a field of view of $34' \times 34'$. Pre-flight per pixel error in the flux was estimated at 20 Gauss (20 Mx cm^{-2}) (Scherrer et al. 1995), which was found to be 14 Gauss in flight as was reported by Hagenaar (2001).

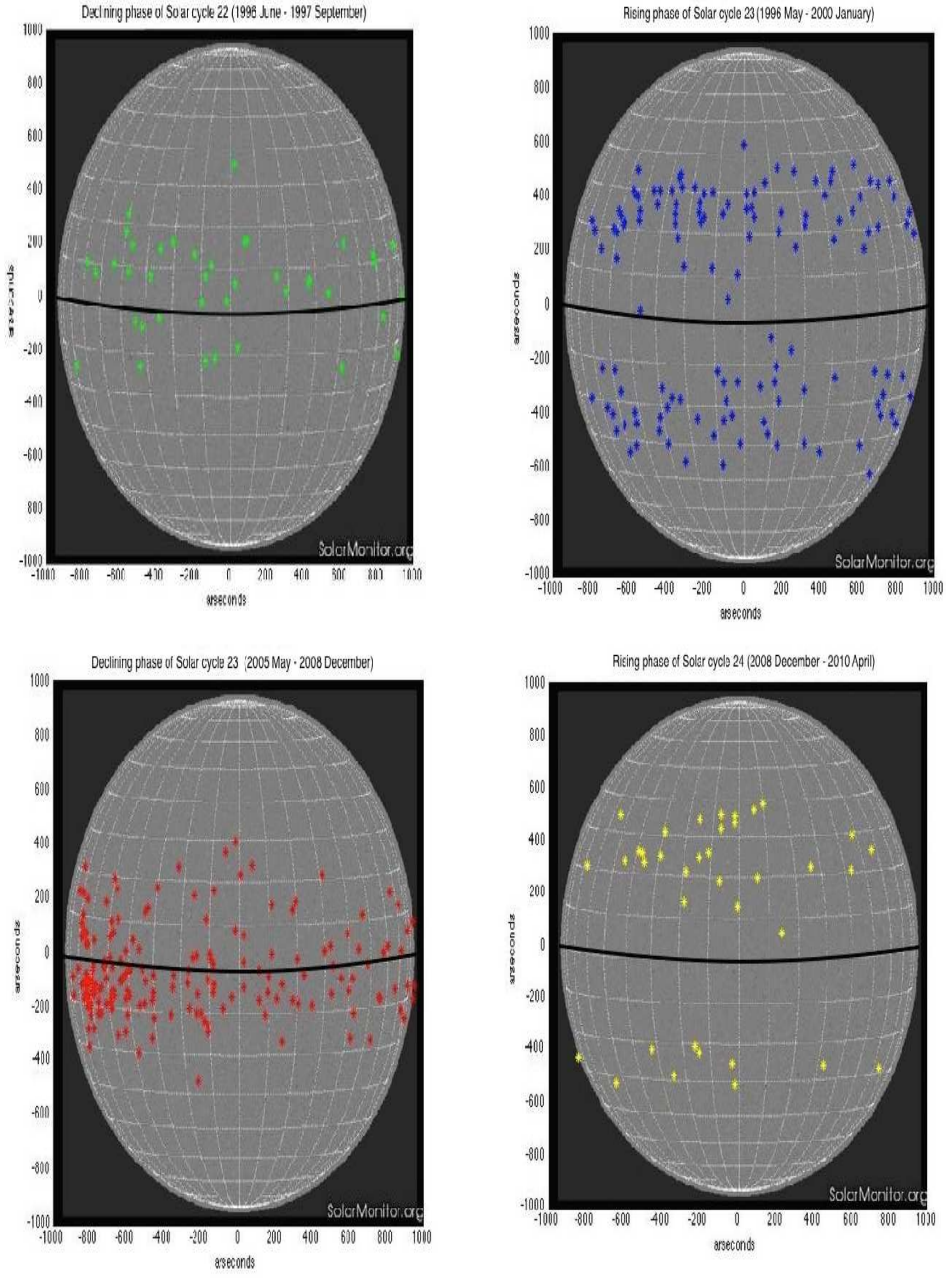
Declining phase of Solar cycle 22 (1996 June - 1997 September)
Rising phase of Solar cycle 23 (1996 May - 2000 January)
Declining phase of Solar cycle 23 (2005 May - 2008 December)
Rising phase of Solar cycle 24 (2008 December - 2010 April)
arseconds
SolarMonitor.org

Fig. 1.— Position of all the active regions formed between 2005 July 22 to 2010 April 12 during decline phase of the solar cycle 22 (top left), rise phase of the solar cycle 23 (top right), decline phase of the solar cycle 23 (bottom left) and rise phase of cycle 24 (bottom right). The location of active region is based on its nomenclature from NOAA database.

In the present work, we have used MDI magnetograms to compute the daily magnetic flux of ARs observed by *solarmonitor.org* on the solar disk from 1996 May 06 to 2010 April 12 (approximately 5100 days) that covers the final stages of the solar cycle 22, the complete cycle 23 and rising phase of the cycle 24. During this period, we have manually monitored evolution of 1948 ARs, which include 286 AR nests and 6 AR evolutions, where dispersion stage of ARs was observed persistent over multiple revolutions. We preferred using a manual approach than an automated one discussed in Zhang et al. (2010) and Stenflo & Kosovichev (2012), so that we could eliminate multiple counting of the same AR due to solar rotation.

Fig. 1 shows the location of ARs on the solar disk during declining phase of the cycle 22 (top left), the rising phase of the solar cycle 23 (top right), the declining phase of the solar cycle 23 (bottom left) and the rising phase of the solar cycle 24 (bottom right). The two hemisphere are separated by black line representing the solar equator. We further represent our observations in a butterfly diagram in Fig. 2 that shows the location of AR observed and the time. Here, in the case of AR nests we have noted the position and date of AR that was first detected in *solarmonitor.org*. We then concentrate our analysis on the 238 ARs observed on the solar disk from 2005 July 22 to 2010 April 12, which covers the declining phase of cycle 23 and the rising phase of cycle 24.

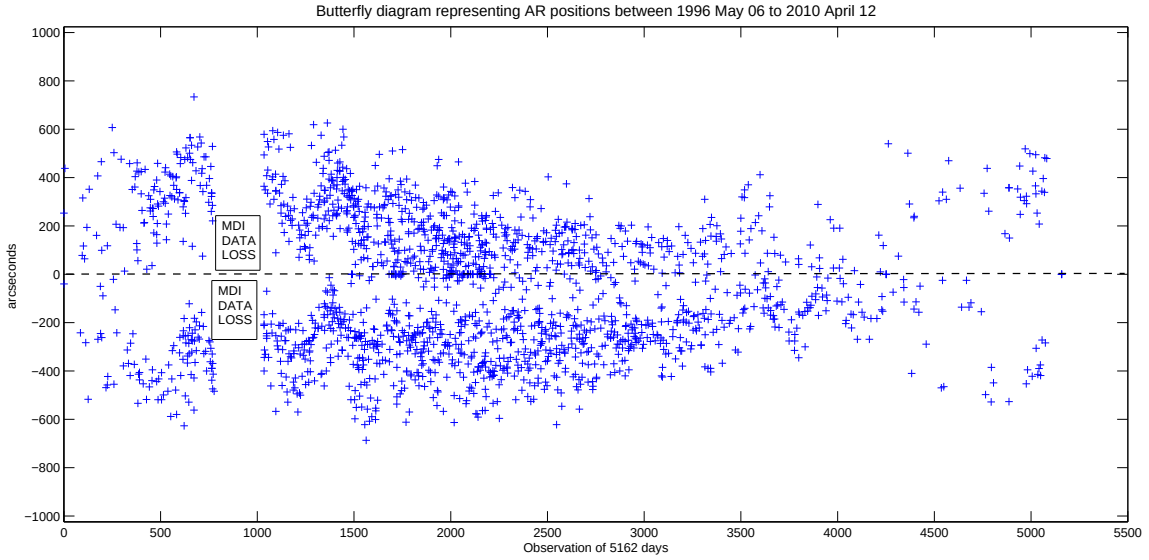

Fig. 2.— A butterfly diagram presenting the position of AR found during 1996 May 06 to 2010 March 10.

To refine the dataset, we ignore those ARs which dispersed in less than two days, since they generally lacked sunspots. We also exclude ephemeral ARs their fluxes are discussed in

Hagenaar (2001) and Hagenaar et al. (2003). The MDI magnetogram shows noise of 0.02″on the limbs, with additional noise on the right limb due to wavelength changes in the Michelson filters Θ (Wenzler et al. 2004). Hence we ignore all ARs born on the right limb at longitudes $\gtrsim 60°$. For ARs born on the right limb with an angle $\gtrsim 60°$the angle between LOS magnetic field and perpendicular magnetic field ($\perp$) tends to zero (Hagenaar 2001; Hagenaar et al. 2003). Hence we have omitted all readings beyond $\gtrsim 60°$.

After choosing the ARs, we select a box containing isolated region/s and calculate the highest value of $B_\perp$ viz. $B_{\perp max}$ in each box. Thereafter we separate the negative and positive polarities of Active Regions, using contours with levels at $B_\perp = 0$, $B_\perp <$ -14 Gauss and $B_\perp >$ 14 Gauss. Then we define a contour at 99 % of the calculated $B_{\perp max}$ values to eliminate the magnetic fields outside the Active Regions. Finally, we use the equation (1) to calculate the magnetic fluxes (Φ) of each regions separately,

$$\Phi = \int B \cdot ds \tag{1}$$

Since the AR magnetic field is bipolar, the net unbalanced magnetic flux in an AR should be nearly zero. To check if our observations were accurate we noted the net unbalanced flux; if it has a value other than zero, then we return to the first step again and reselect the boxes. This parameter also meant that we consider AR nest as single large AR that occurred mostly during maximum of solar cycle 23. During the minima we found two AR nests and were able to resolve them into individual ARs. In order to remove the error due to line-of-sight (LOS) effects, we calculate the angle Θ of each pixel from the disk center following method described in Hagenaar (2001) using:

$$\Theta = \sin^{-1}[\frac{\sqrt{(\ {x_\perp}^2\ ) + (\ {y_\perp}^2\ )}}{R}] \tag{2}$$

(where $x_\perp$, $y_\perp$ are radial co-ordinates of each pixel within the active region on the solar disk and R is the radius of Sun in pixels).

To calculate the LOS magnetic flux of ARs, we have used the relation that LOS magnetic flux is related to perpendicular component of magnetic flux using the formula

$$\Phi_{LOS} = \Phi_\perp \cdot \cos\Theta. \tag{3}$$

3. Analysis and results related to the deep minima

In order to understand magnetic flux evolution, we produce magnetic flux vs time graphs as shown in Fig. 3 and Fig. 4. We summarise the calculated fluxes from the complete database in the Fig. 3. We represent fluxes from NOAA 07961 as 0 (1996 May 06) on the x-axis as the beginning of the dataset and proceed with computing daily fluxes. Since we intended to study both hemispheres independently, we have represented AR fluxes in the northern hemisphere by black solid lines and southern hemisphere by red solid lines. It can be easily noticed from Fig. 3 that the solar cycle 23 was significantly asymmetric in terms of dominating hemispheres.

Stenflo & Kosovichev (2012) and Zhang et al. (2010), have carried detailed analysis of active regions observed by MDI with their respective techniques. Stenflo & Kosovichev (2012), performed critical analysis of dataset using automated techniques and studied various properties of these bipolar regions including their orientation including the tilt angle variation. Zhang et al. (2010), on the other hand studied the basic physical parameters including the magnetic flux of individual active regions, their distribution with respect to size as well as magnetic flux. They found the solar cycle between 1996 and 2008 very asymmetric. In terms of number of ARs, they found 938 ARs in the South and 792 in the North. We found similar results, we found 1071 AR in the South and 872 in the North, which makes the asymmetry approximately 12 %. Zhang et al. (2010) also studied the asymmetry in the magnetic flux and found that the Southern hemisphere was stronger than the Northern hemisphere during the declining phase of the solar cycle 23, we found a similar asymmetry where we found 10 times more flux emergence in the Southern hemisphere. These results are also in agreement with those obtained by (Li et al. 2009) and (Chowdhury et al. 2013), based on sunspot observations.

Fig. 3 suggest that the behaviour of deep minima may be related to AR fluxes related to the later part of the declining phase of the cycle 23. Thus we concentrate our analysis on the latter part of the cycle 23. In order to study the flux behaviour therein, we selected final 1694 days from Fig. 3 (i.e. data between 3468^{th} day to 5162^{th} day) and represented in the graphs in Fig. 4. Here, we represent our observations with NOAA AR 10791 (northern hemisphere, observed on 2005 July 22 and represented by 0 on the x-axis in the top panel of Fig. 4). In the South we began with NOAA AR 10794 (southern hemisphere, observed on 2005 August 01), both occurring roughly mid-way during the declining phase of cycle 23. We continue until the dispersion of NOAA AR 11060 (in the northern hemisphere on 2010 April 12 represented by 1694 on the x-axis in Fig. 4) in the North. In the plots, blue line indicates the magnetic flux behaviour during the declining phase of cycle 23 and the black line indicates the magnetic flux behaviour during the rising phase of cycle 24.

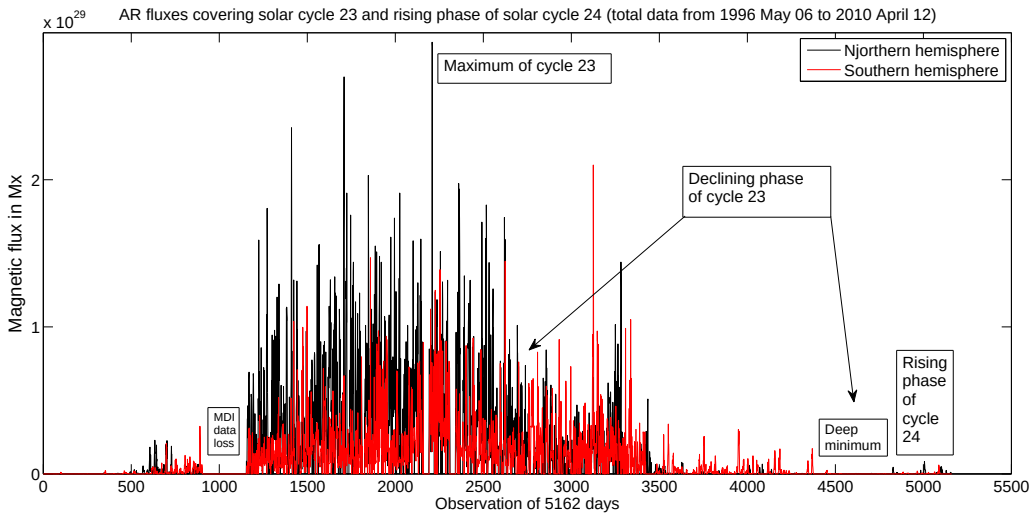

Fig. 3.— Comparison of AR flux behaviour between the northern and the southern hemispheres from the 1996 May 06 to 2010 March 10.

Fig. 4 clearly indicates that photospheric magnetic flux during the final four years of solar cycle 23 was dominant in the southern hemisphere, producing a profound north-south asymmetry in terms of AR numbers and magnetic flux. During this period we found 121 ARs in the Southern hemisphere as compared to 60 ARs in the Northern hemisphere. This asymmetry becomes even more pronounced as the cycle progresses. The AR fluxes in the southern hemisphere were approximately 10 times stronger than those in the northern hemisphere. But this behaviour changed completely during the rising phase of cycle 24, for which the strength of fluxes in the North is 4 times that of the South. This was observed with 36 ARs emerging in the North compared to 23 in the South. Proceeding towards cycle 24, we find that (see Fig. 4) the new cycle began in the North on the 875 th day, which is 2007 December 13 with the emergence of opposite polarity sunspot was observed. In the South the opposite polarity sunspot was observed on 1013^{th} day, which is 2008 May 3. This is 143 days (about 5 months) after the reversal of polarities in northern hemisphere. Moreover, Fig. 4 also clearly shows that the change of polarity in the northern hemisphere occurred smoothly and quickly, with a mixture of ARs from both cycles for a period of 200 days, whereas in the southern hemisphere, the new emerging flux showed a delay.

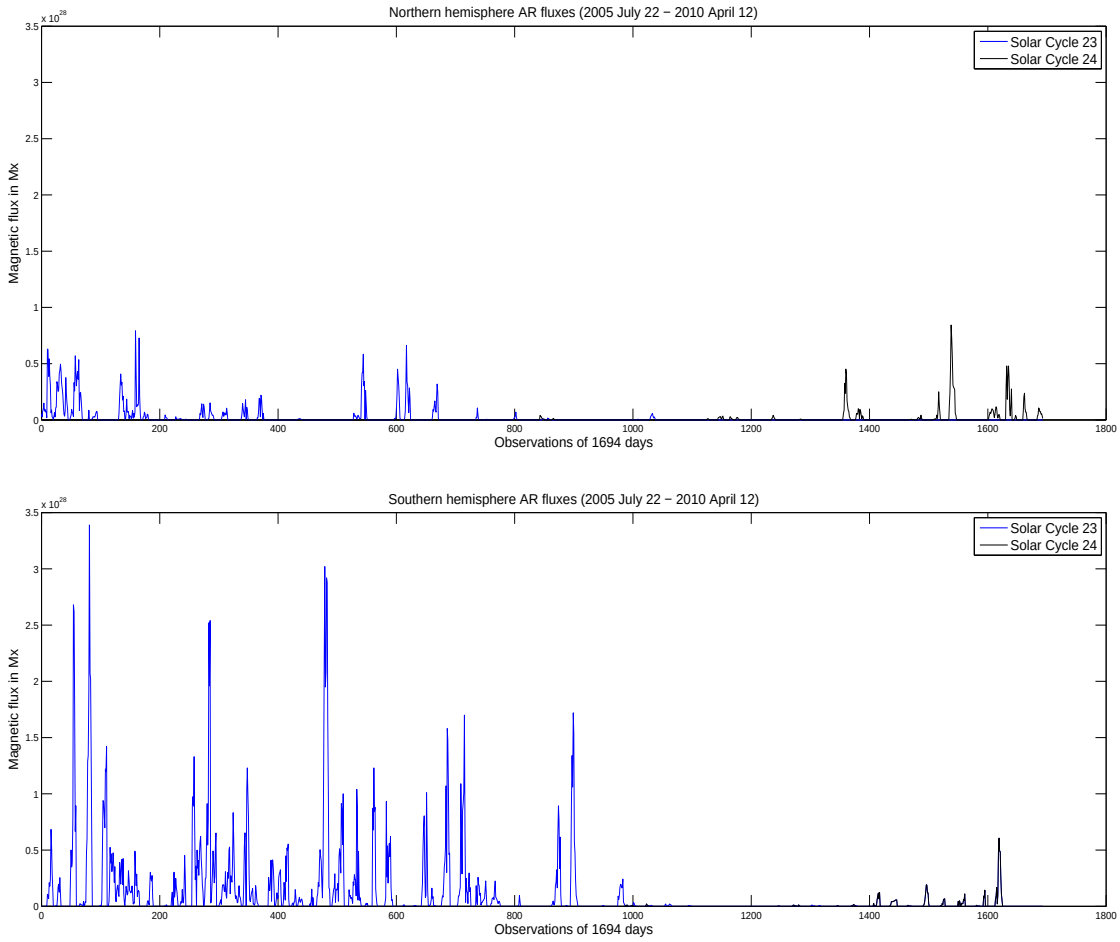
Northern hemisphere AR fluxes (2005 July 22 − 2010 April 12)
x 10^28
Magnetic flux in Mx
Observations of 1694 days
Solar Cycle 23
Solar Cycle 24
Southern hemisphere AR fluxes (2005 July 22 − 2010 April 12)
x 10^28
Magnetic flux in Mx
Observations of 1694 days
Solar Cycle 23
Solar Cycle 24

Fig. 4.— AR flux behaviour during the deep minimum, the upper panel shows flux behaviour in the Northern hemisphere and the lower panel shows AR flux behaviour in the Southern hemisphere. The graphs clearly indicate the difference in strengths of magnetic fluxes in both the cycles.

4. North-South asymmetries from dynamo action

In order to understand how the solar dynamo works and to investigate the reason behind our observational results concerning the asymmetry between hemispheres, and to understand the effect of this asymmetry on the deep minima, we have carried out sets of dynamo simulations. Belucz & Dikpati (2013) have shown that differences in the form and amplitude of meridional circulation between North and South hemispheres can cause significant differences in the poloidal, polar and toroidal fields produced there. The longer the meridional circulation differences persisted, the larger the differences became. Belucz & Dikpati (2013) focussed on global changes in meridional circulation, including amplitude changes of the whole circulation, differences between one and two cells in either latitude or depth. The meridional motions of sunspots, pores (Ribes & Bonnefond 1990, and their citations) and other magnetic features (Komm 1994; Meunier 1999) are related to generation of inflows. Observations by Gizon & Birch (2005) show that there are also significant meridional circulation patterns in the Sun that are not global, including one that is associated with ARs themselves. In particular, there are inflows into ARs from lower and higher latitudes that can be as large as 50 m s^{-1}. When averaged in longitude, these inflows can create a meridional circulation signal of 5 m s^{-1} or more. With more active regions in one hemisphere compared to the other, the average inflow should also be larger in the more active hemisphere. In addition, since ARs are the source of surface poloidal flux that migrates toward the poles and causes polar field reversals, the effect of the meridional circulation from the inflows may in fact be larger than represented by the full longitude average. It has also been shown that the inflows may play an important role in the generation of poloidal field during the final stages of the solar cycle (Cameron & Schüssler 2012; Jiang et al. 2010). Therefore, we need to assess the role of active region inflows and their differences between North and South hemispheres to see how much difference in solar cycles they can produce.

We have carried out flux-transport dynamo simulations using the same model as used in Belucz & Dikpati (2013), in order to see the role of active region inflows. For the sake of completeness, we briefly repeat the set-up of the simulation runs in the following subsection (§4.1), which describes the dynamo equations, mathematical forms of the dynamo ingredients and boundary and initial conditions. The subsection §4.2 presents the detailed formulation of the treatment of inflow cells, and §4.3 the consequences of the inflow cells.

4.1. Dynamo simulation set-up

Our starting point is the set-up of Belucz & Dikpati (2013). We write the dynamo equations as:

$$\frac{\partial A}{\partial t}+\frac{1}{r\sin\theta}(\mathbf{u}.\nabla)(r\sin\theta A)=\eta(\nabla^2-\frac{1}{r^2\sin^2\theta})A+[S_{\rm BL}(r,\theta)+S_{\rm tac}(r,\theta)]$$
$$\times\left[1+\left(\frac{B_\phi|_{ov}(\theta,t)}{B_0}\right)^2\right]^{-1}B_\phi|_{ov}(\theta,t), \quad (4a)$$

$$\frac{\partial B_\phi}{\partial t}+\frac{1}{r}\left[\frac{\partial}{\partial r}(ru_rB_\phi)+\frac{\partial}{\partial\theta}(u_\theta B_\phi)\right]=r\sin\theta(\mathbf{B}_p.\nabla)\Omega-\hat{\mathbf{e}}_\phi\,.\,[\nabla\eta\times\nabla\times B_\phi\hat{\mathbf{e}}_\phi]$$
$$+\eta(\nabla^2-\frac{1}{r^2\sin^2\theta})B_\phi, \quad (4b)$$

in which $A(r,\theta,t)$ denotes the vector potential for the poloidal field, $B_\phi(r,\theta,t)$ the toroidal field, $u_r(r,\theta)$, $u_\theta(r,\theta)$ the meridional flow components, $\Omega(r,\theta)$ the differential rotation, $\eta(r)$ the depth-dependent magnetic diffusivity, $S_{\rm BL}(r,\theta)$ the Babcock-Leighton type surface poloidal source, $S_{\rm tac}(r,\theta)$ the tachocline α-effect and B_0 the quenching field strength, which we set to 10 kGauss in this calculation.

We use the following expressions respectively for Babcock-Leighton surface source and tachocline α-effect:

$$S_{\rm BL}(r,\theta)=\frac{s_1}{4}\left[1+{\rm erf}\left(\frac{r-r_1}{d_1}\right)\right]\left[1-{\rm erf}\left(\frac{r-r_2}{d_2}\right)\right]\,2\,\sin\theta\cos\theta. \quad (5)$$

For $0\le\theta\le\pi/2$,

$$S_{\rm tachocline}(r,\theta)=\frac{s_2}{4}\left[1+{\rm erf}\left(\frac{r-r_3}{d_3}\right)\right]\left[1-{\rm erf}\left(\frac{r-r_4}{d_4}\right)\right].\frac{\sin\left(6(\theta-\frac{\pi}{2})\right)e^{-\gamma_2\,(\theta-\frac{\pi}{4})^2}}{[e^{\gamma_3(\theta-\pi/3)}+1]}, \quad (6a)$$

and, for $\pi/2\le\theta\le\pi$,

$$S_{\rm tachocline}(r,\theta)=\frac{s_2}{4}\left[1+{\rm erf}\left(\frac{r-r_3}{d_3}\right)\right]\left[1-{\rm erf}\left(\frac{r-r_4}{d_4}\right)\right].\frac{\sin\left(6(\theta-\frac{\pi}{2})\right)e^{-\gamma_2\,(\theta-\frac{3\pi}{4})^2}}{[e^{\gamma_3(2\pi/3-\theta)}+1]}. \quad (6b)$$

The parameter values used in (5), (6a) and (6b) are: $s_1=2.0\,{\rm ms}^{-1}$, $s_2=0.5\,{\rm ms}^{-1}$, $r_1=0.95R_\odot$, $r_2=0.987R_\odot$, $r_3=0.705R_\odot$, $r_4=0.725R_\odot$, $d_1=d_2=d_3=d_4=0.0125R_\odot$, $\gamma_2=70.0$, $\gamma_3=40.0$. Note that the values of s_1 and s_2 determine the amplitude of the Babcock-Leighton poloidal source term and the tachocline α-effect respectively, but the maximum amplitudes of $S_{\rm BL}$ and $S_{\rm tachocline}$ are not exactly $2\,{\rm ms}^{-1}$ and $50\,{\rm cms}^{-1}$, but instead $\sim 1.93\,{\rm ms}^{-1}$ and $\sim 37\,{\rm cms}^{-1}$ respectively, for the parameter choices given above. This happens due to the modulation of error functions used in expressions (5), (6a) and (6b).

The diffusivity profile is given by (7) (for more details, see Dikpati et al. (2002).

$$\eta(r) = \eta_{\rm core} + \frac{\eta_{\rm T}}{2}\left[1 + {\rm erf}\left(\frac{r - r_5}{d_5}\right)\right] + \frac{\eta_{\rm super}}{2}\left[1 + {\rm erf}\left(\frac{r - r_6}{d_6}\right)\right], \tag{7}$$

in which, $\eta_{\rm core} = 10^9\,{\rm cm^2 s^{-1}}$, $\eta_{\rm T} = 7 \times 10^{10}\,{\rm cm^2 s^{-1}}$, $\eta_{\rm super} = 3 \times 10^{12}\,{\rm cm^2 s^{-1}}$, $r_5 = 0.7 R_\odot$, $r_6 = 0.96 R_\odot$, $d_5 = 0.00625 R_\odot$, $d_6 = 0.025 R_\odot$. These choices make this profile possess a supergranular type diffusivity value ($\eta_{\rm super}$) in a thin layer at the surface, which drops to a turbulent diffusivity value ($\eta_{\rm T}$) in the bulk of the convection zone, and at the base of the convection zone the diffusivity drops quite sharply to a much lower value ($\eta_{\rm core}$) to mimic the molecular diffusivity.

The stream function ψ for the steady part of the meridional circulation is given by:

$$\psi r \sin\theta = \psi_0 \frac{(\theta - \theta_0)}{(\theta + \theta_0)} \sin\left[k\frac{\pi(r - R_b)}{(R_\odot - R_b)}\right]\left(1 - e^{-\beta_1 r \theta^\epsilon}\right)\left(1 - e^{\beta_2 r(\theta - \pi/2)}\right) e^{-((r - r_0)/\Gamma)^2}. \tag{8}$$

The streamline flow can be obtained in the North hemisphere by plotting the contours of $\psi\, r\, \sin\theta$. The streamlines in the South hemisphere can be obtained by implementing mirror symmetry about the equator. This parameter values for this stream function are: $k = 1$, $R_b = 0.69R$, $\beta_1 = 0.1/(1.09 \times 10^{10})\,{\rm cm^{-1}}$, $\beta_2 = 0.3/(1.09 \times 10^{10})\,{\rm cm^{-1}}$, $\epsilon = 2.00000001$, $r_0 = (R_\odot - R_b)/5$, $\Gamma = 3 \times 1.09 \times 10^{10}\,{\rm cm}$ and $\theta_0 = 0$. This choice of the set of parameter values produce a flow pattern that peaks at 24° latitude.

In order to perform simulations in non-dimensional units, we use $1.09 \times 10^{10}\,{\rm cm}$ as the dimensionless length and $1.1 \times 10^8\,{\rm s}$ as the dimensionless time. These choices respectively come from setting the dynamo wavenumber, $k_D = 9.2 \times 10^{-11}\,{\rm cm^{-1}}$, as the dimensionless length, and the dynamo frequency, $\nu = 9.1 \times 10^{-9}\,{\rm s^{-1}}$, as the dimensionless time, which means that the dynamo wavelength ($2\pi \times 1.09 \times 10^{10}\,{\rm cm}$) is 2π and the mean dynamo cycle period (22 years) is 2π in our dimensionless units. Thus, in non-dimensional units, the parameters that define the meridional circulation given in the expression (5) are: $R_b = 4.41$, $\beta_1 = 0.1$, $\beta_2 = 0.3$, $\epsilon = 2.00000001$, $r_0 = (R_\odot - R_b)/5$, $\Gamma = 3$ and $\theta_0 = 0$. The latitude of the peak flow can be varied by changing β_1 and β_2; for example, changing β_1 from 0.1 to 0.8 and β_2 from 0.3 to 0.1, a flow pattern can be constructed that peaks at 50°, but for the present study, we fix the latitude of the peak flow at 24°.

Considering an adiabatically stratified solar convection zone, we take the density profile as,

$$\rho(r) = \rho_b[(R_\odot/r) - 1]^m, \tag{9}$$

in which $m = 1.5$. However, in order to avoid density vanishing at $r = R_\odot$, which would cause an unphysical infinite flow at the surface, we use $\rho(r) = \rho_b[(R_\odot/r) - 0.97]^m$ in our simulations. Using the constraint of mass-conservation, the velocity components (v_r, v_θ) can be computed from

$$u_r = \frac{1}{\rho r^2 \sin\theta}\frac{\partial}{\partial\theta}(\psi r \sin\theta), \tag{10a}$$

$$u_\theta = -\frac{1}{\rho r \sin\theta}\frac{\partial}{\partial r}(\psi r \sin\theta). \tag{10b}$$

The peak flow speed is determined by a suitable choice of ψ_0/ρ_b. We use a peak flow speed of $14\,\mathrm{ms}^{-1}$ in all simulations.

4.2. Formulation of inflow cells

In order to include inflow cells into the steady meridional circulation pattern, described in §4.1, we incorporate a time-dependent stream function ($\Psi_{\rm inflow}$), which is prescribed as follows:

$$\Psi_{\rm inflow} = \psi_{0_{\rm inflow}} \sin\left[\frac{\pi(r - r_{\rm inflow})}{(R_\odot - r_{\rm inflow})}\right] \sin\left[\frac{2\pi(\theta - \theta_{\rm high})}{(\theta_{\rm low})}\right]. \tag{11}$$

In expression (11), $\psi_{0_{\rm inflow}}$ determines the velocity amplitude of the inflow cells, $r_{\rm inflow}$ determines how deep down the inflow cells extend from the surface, $\theta_{\rm high}$ and $\theta_{\rm low}$ determine their extent in θ (colatitude) coordinate, $\theta_{\rm high}$ denoting the cell-boundary at the poleward side and $\theta_{\rm low}$ the equatorward side. Since the inflow cells are normally associated with active regions, their θ locations have to be function of time. We implement the time-dependence in the θ coordinate of the inflow cells in accordance with the migration of latitude-zone of sunspots. Thus we prescribe $\theta_{\rm high}$ and $\theta_{\rm low}$ as follows:

$$\theta_{\rm high} = \theta_{\rm center} - \pi/18, \tag{12a}$$

$$\theta_{\rm low} = \theta_{\rm center} + \pi/18, \tag{12b}$$

$$\theta_{\rm center} = \theta_{\rm center_{initial}} + \delta t\frac{\pi/6}{\tau}. \tag{12c}$$

Here $\theta_{\rm center}$ is the center of the inflow cells, $\theta_{\rm center_{initial}}$ is the starting location of the center of the inflow cells and $\frac{\pi/6}{\tau}$ is the migration speed of the center of the inflow cells. Note that the θ-extent of each of the pair of inflow cells is 10°. So in order to make the inflow cells migrate from $\sim 50°$ latitude to the equator, we have to make their center migrate from $\sim 40°$ latitude to $\sim 10°$ latitude. Here τ is approximately one sunspot cycle period (i.e. half of a magnetic

cycle period), and δt is the time-step for dynamo field evolution. For simplicity, we assume in this calculation that their extent in depth remains the same. We take $r_{\rm inflow} = 0.9\_R_\odot$.

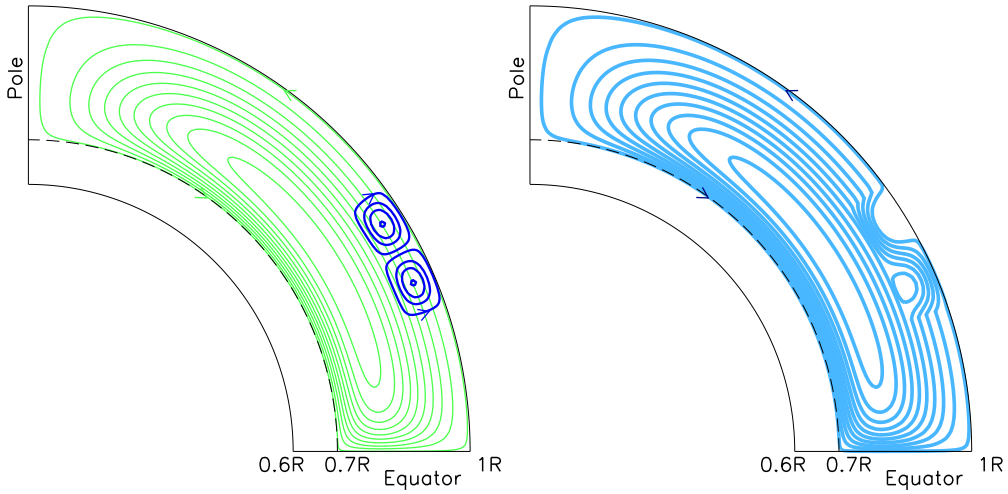

Fig. 5.— Left image: Green streamlines show mean meridional circulation and on top of green streamlines inflow cells are separately plotted in blue. Right image shows the total flow pattern due to mean flow and inflow cells.

Fig. 5 shows the prescribed form of the inflow circulation cells (see expressions 11, 12a-c) we have included in the dynamo model. In left panel we have superimposed the inflow circulation streamlines on the single celled global meridional circulation. As mentioned earlier, in our calculations we have allowed the inflow circulation to reach to a depth of 0.9 $R\odot$ and to latitudes of 10° poleward and equator-ward of the active region latitude. The right panel in Fig. 5 shows the total streamlines for a case for which the peak global circulation is 14 m s^{-1} and the peak inflow is 15 m s^{-1}.

4.3. Effect of north-south asymmetry in inflow cells

In the simulations, the inflow pattern is introduced into both North and South hemispheres, but with a much stronger peak in the South (15 m s^{-1} in the South versus 1.5 m s^{-1} in the North). The choice of this difference is motivated by the fact that there were many more active regions in the South compared to the North in the declining phase of cycle 23 (see Fig. 1) and the flux in the southern hemisphere was observed to be about a factor of 10 higher than in the northern hemisphere. In both hemispheres, the inflow circulation pattern is propagated toward the equator at a rate consistent with the equator-ward migration of the latitudes of active region appearance. Fig. 6 shows the patterns of meridional circulation

(panels a-d), toroidal field contours (panels e-h) and poloidal field lines (panels i-l) for a sequence of time intervals separated by 2.7 yr within a single sunspot cycle. The simulation was begun a few cycles earlier with the same weak inflow in both hemispheres; the stronger inflow in the South was introduced a few months before the first frames shown.

We see in panel (i) there is an immediate effect on the surface poloidal field in the South. By counting the number of contours of poloidal field lines, we can see this effect in the form of more concentrated flux in the neighbourhood of the inflow pattern. Because the extra inflow near the surface is slowing down the migration of poloidal flux toward the pole, by panel (j) 2.7 years later, the polar field in the South is weaker and is reversing sign later than in the North. Again the number of contours reveals that this results in less poloidal flux being transported to the bottom in high latitudes to cancel out the previous poloidal fields. This, in turn allows the toroidal field near the bottom in the South to become significantly stronger than in the North (see panels f,g,h). Therefore we see that the stronger inflows associated with one cycle in one hemisphere can lead to stronger toroidal fields in that hemisphere in the next cycle. This suggests that in the nearly independent North and South hemispheres the strength of one hemisphere compared to the other may persist for more than one cycle. There is observational evidence for this persistence, which is discussed in Dikpati et al. (2007, and reference therein) as well as differences in time of sunspot maximum.

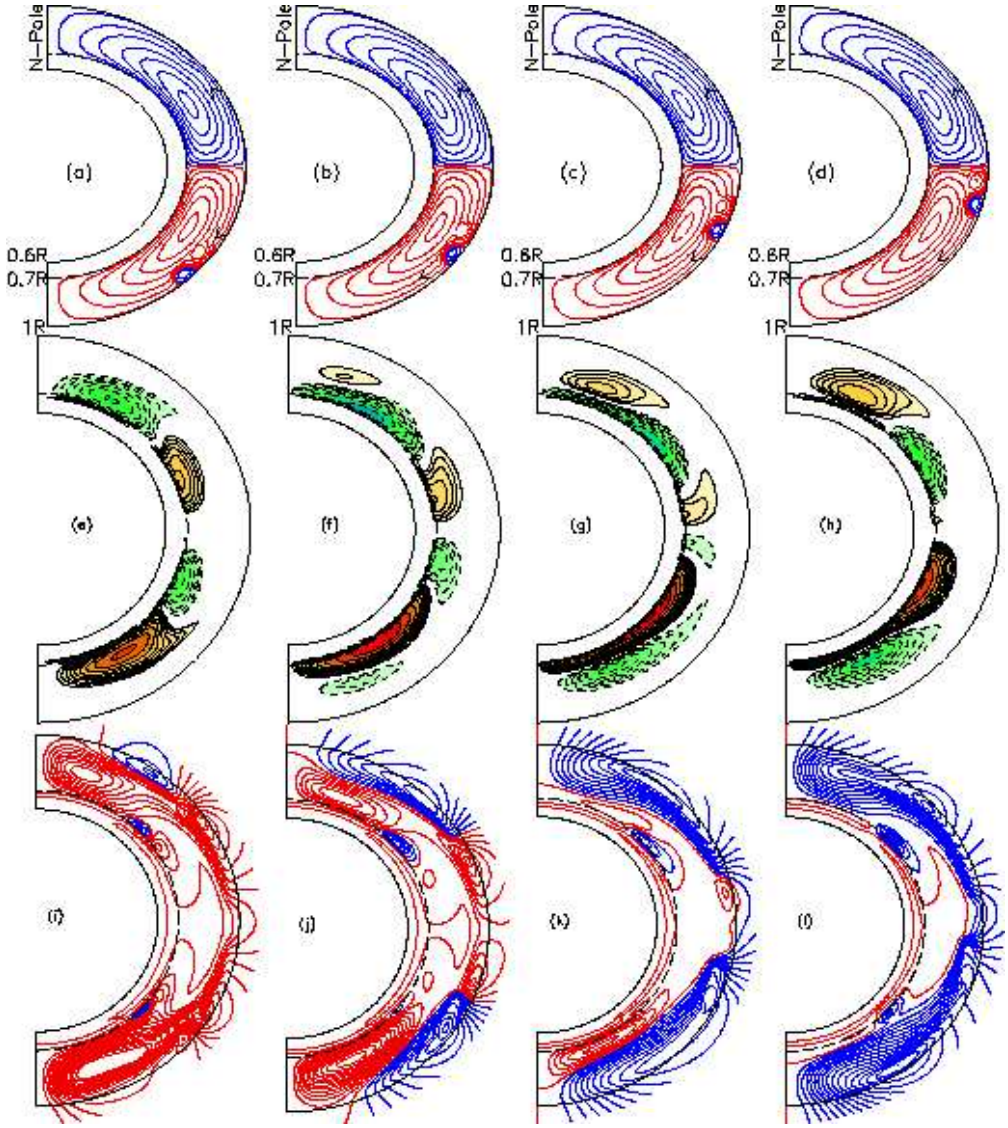

Fig. 6.— Top panels (a-d): Snapshots of streamlines at four epochs within a sunspot cycle due to drifting of inflow cells from mid-latitude to the equator. Note that the South has stronger inflow cells in this simulation. Middle panels (e-h) show the snapshots of dynamo-generated toroidal fields at the same four epochs; red denotes positive field (going into the plane of the paper) and blue negative field (coming out of the plane of the paper). Bottom panels (i-l) show the poloidal field lines; red denote positive (clockwise) and blue negative (anticlockwise).

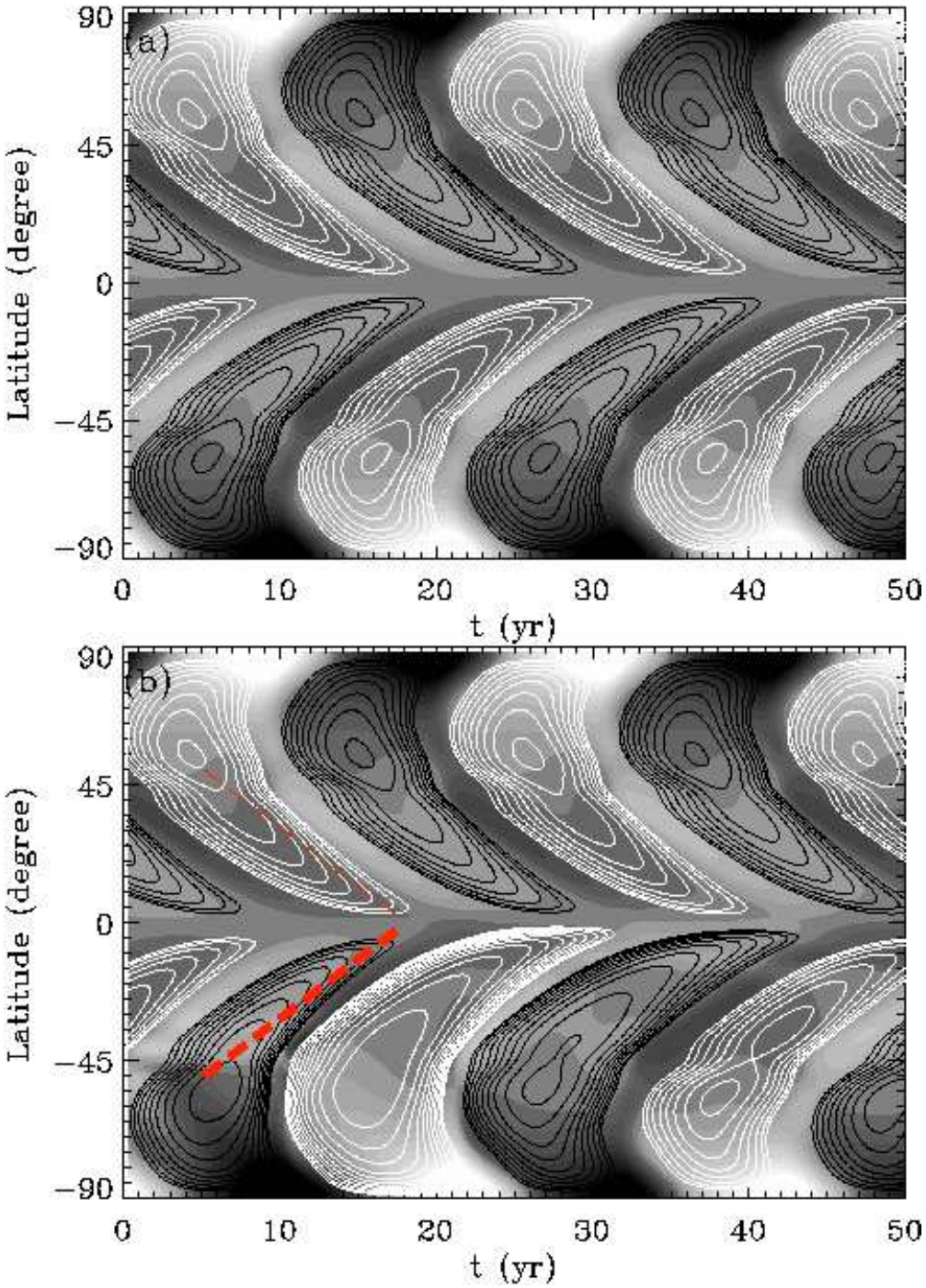

Fig. 7.— Top panel (a): Time-latitude diagram of toroidal fields (black-white contours) taken from the base of the convection zone, and surface radial fields (greyscale map) for weak inflow cells of 1.5 m/s speed in both hemispheres. Bottom panel (b): Same as in (a) but for 10 times stronger inflow cell in the South compared to the North. The locus of inflow cells are shown in red-dashed lines; a relatively thicker line in the South denotes stronger inflow cells as incorporated in this simulation.

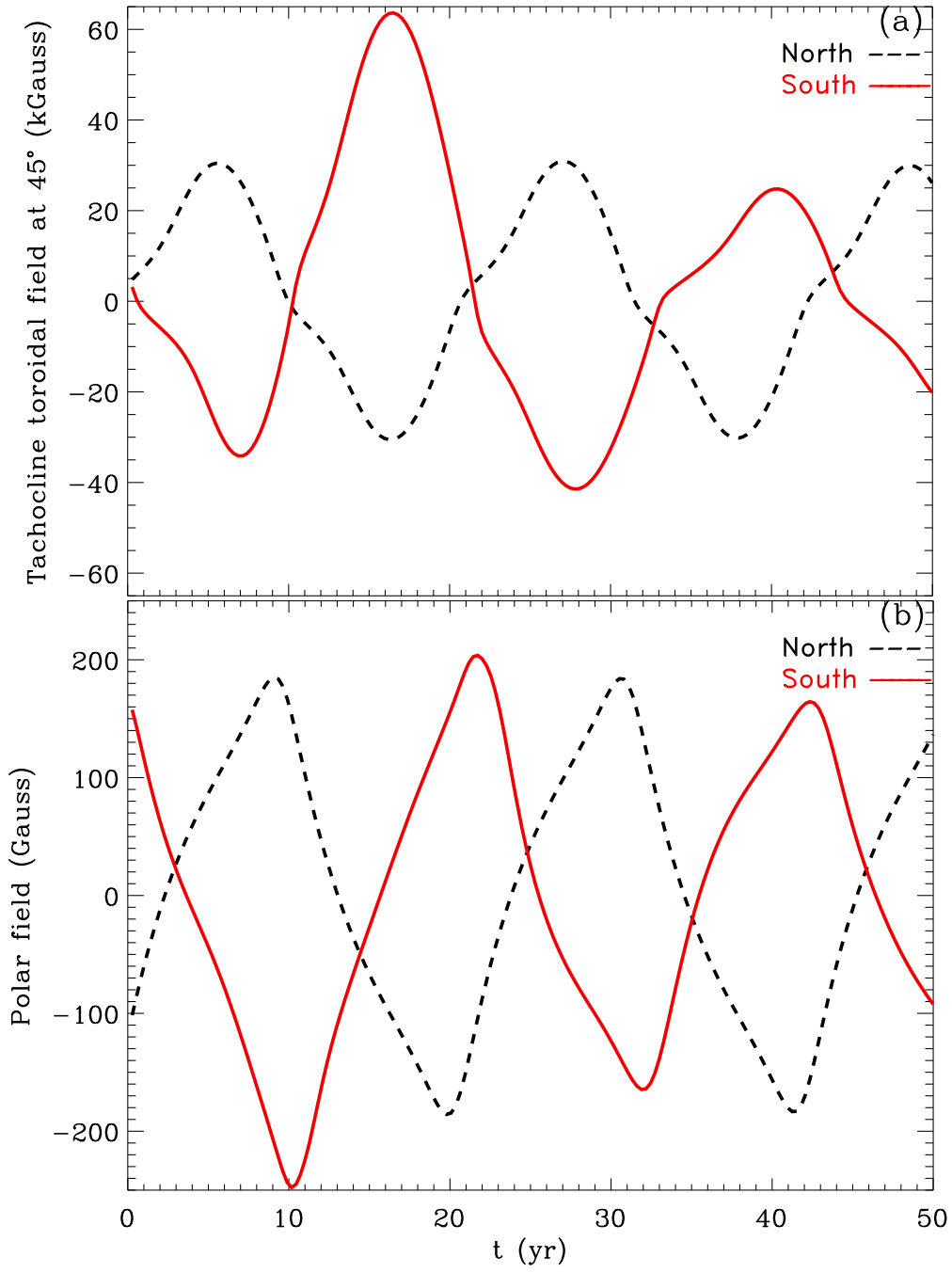

Fig. 8.— Top image: Tachocline toroidal fields taken from 45° latitude in North (dashed black) and South (solid red) as function of time. Bottom image: Polar fields in North (dashed black) and South (solid red).

In this particular simulation, the difference in inflow speed was introduced for a duration of about 12 years, after which the inflow in the South returned to the same lower value as in the North. Fig. 7 shows a butterfly diagram for several cycles that includes the time with different inflows. On this diagram the extra inflow in the South occurred for years 5-17. Shading is for the poloidal field amplitudes, contours for the toroidal field amplitude. If we focus on the toroidal field contours, we can see that the stronger toroidal field in the South persists for more than one cycle after the extra inflow has been switched off. This effect can clearly be seen in Fig. 8, in which the tachocline toroidal fields, taken from 45° latitude, have been plotted in the North (dashed black) and South (solid red) in the top frame. In the bottom frame the polar field patterns in the North (dashed black) and South (solid red)are presented. The effect of even a temporary increase in inflow affects the dynamo well beyond the duration of the extra inflow; even though the maximum effect on the polar field, namely a continuous increase in the South polar field can be seen during the drifting inflow cells until the sunspot minimum, the effect on the tachocline toroidal fields is more enhanced in the succeeding cycle, because of the increased polar fields being advected there by the time of the start of the next sunspot cycle, thus providing a stronger seed magnetic field. Cameron & Schüssler (2012) found a similar effects, namely an increase in polar field at the end of a sunspot cycle and an increase in the sunspot cycle strength in the succeeding cycle, due to the presence of inflow cells in their surface transport model. In reality the extra inflow would persist as long as more ARs are produced in the South, so the effect of this extra inflow would be even more pronounced and persistent, and inherently nonlinear.

5. Summary and Discussion

The peculiar behaviour of the solar cycle 23 and its prolonged minima has attracted much attention of the researchers over the last few years. There have been various studies taking very many different parameters into account. In the present paper we have discussed the contribution of AR's fluxes and their asymmetries in the north-south hemispheres, during the solar cycle 23 and rising phase of solar cycle 24 with the aim to address the issue of the deep minimum observed in the solar cycle 23. The observations showed that the cycle 23 was highly asymmetric. During the rise phase of the cycle 23, the northern hemisphere was dominant over the southern hemisphere which reversed during the decline phase of the cycle.

Further we concentrated our analysis on the declining phase of the cycle 23 and rising phase of the cycle 24. The analysis shows that the magnetic flux in the southern hemisphere is about 10 times stronger than that in the northern hemisphere during the declining phase of the solar cycle 23. The trend, however, reversed during the rising phase of the solar cycle 24

and magnetic flux becomes more stronger (about a factor of 4) in the northern hemisphere. Moreover, it was found that there was significant delay (about 5 months) in changing the polarity in southern hemisphere in comparison with the northern hemisphere. These results may provide us with hints about how the toroidal fluxes would have contributed to the solar dynamo during the prolonged minima in the solar cycle 23 and in the rise phase of the solar cycle 24.

It has been shown previously by Belucz & Dikpati (2013) that the degree of asymmetry in amplitude between North and South hemispheres can be changed significantly by differences in meridional circulation amplitude and/or profile between North and South. Here we have demonstrated that the difference between hemispheres in axisymmetric inflow into active region belts can lead to differences in peak amplitude that can last for more than one sunspot cycle. In the example shown here, we find that an increase in inflow in the South, which would accompany more solar activity there, leads to stronger toroidal fields in the South for substantially more than one cycle even after the extra inflow has been shut off. Therefore this mechanism can lead to persistence of one hemisphere dominating over the other for multiple cycles, as is often observed. In effect, once a larger inflow is established in one hemisphere, its existence provides reinforcement for stronger cycles in that hemisphere to follow. An interesting question is then how the Sun eventually breaks out of this asymmetric pattern to a new one in which the other hemisphere dominates. Among other possibilities, this could occur when some other feature of meridional circulation, such as its amplitude or profile, changes in one hemisphere relative to the other.

Acknowledgements: We thank the referee for important inputs which has made the manuscript more comprehensive. Authors would like to thank Robert Cameron for valuable inputs on the manuscript. Juie Shetye thanks IUCAA for the excellent hospitality during her visit. This project was started at IUCAA. We gratefully acknowledge the Prof. John Gerard Doyle at Armagh Observatory for the important correction and suggestions. Research at Armagh Observatory is grant-aided by the Leverhulme Trust, Grant Ref: RPG-2013-014 and the work at High Altitude Observatory, National Center for Atmospheric Research Boulder is partially supported by NASA's LWS grant with award number NNX08AQ34G. The National Center for Atmospheric Research is sponsored by the National Science Foundation. SOHO is a project of international cooperation between ESA and NASA.

REFERENCES

Ataç, T., & Özgüç, A. 1996, Sol. Phys., 166, 201

Babcock, H. W. 1961, ApJ, 133, 572

Belucz, B., & Dikpati, M. 2013, ApJ, 779, 4

Cameron, R. H., & Schüssler, M. 2012, A&A, 548, A57

Carbonell, M., Oliver, R., & Ballester, J. L. 1993, A&A, 274, 497

Choudhuri, A. R., Schussler, M., & Dikpati, M. 1995, A&A, 303, L29

Chowdhury, P., Choudhary, D. P., & Gosain, S. 2013, ApJ, 768, 188

Dikpati, M., Corbard, T., Thompson, M. J., & Gilman, P. A. 2002, ApJ, 575, L41

Dikpati, M., de Toma, G., Gilman, P. A., Arge, C. N., & White, O. R. 2004, ApJ, 601, 1136

Dikpati, M., Gilman, P. A., de Toma, G., & Ghosh, S. S. 2007, Sol. Phys., 245, 1

Gao, P.-X., Li, K.-J., & Shi, X.-J. 2009, MNRAS, 400, 1383

Gizon, L., & Birch, A. C. 2005, Living Reviews in Solar Physics, 2, 6

Goel, A., & Choudhuri, A. R. 2009, Research in Astronomy and Astrophysics, 9, 115

Hagenaar, H. J. 2001, ApJ, 555, 448

Hagenaar, H. J., Schrijver, C. J., & Title, A. M. 2003, ApJ, 584, 1107

Jiang, J., Işik, E., Cameron, R. H., Schmitt, D., & Schüssler, M. 2010, ApJ, 717, 597

Knaack, R., Stenflo, J. O., & Berdyugina, S. V. 2004, A&A, 418, L17

—. 2005, A&A, 438, 1067

Komm, R. W. 1994, Sol. Phys., 149, 417

Krainev, M. B. 2012, Bulletin of the LEbdev Physics Institute, 39, 95

Li, K. J., Chen, H. D., Zhan, L. S., Li, Q. X., Gao, P. X., Mu, J., Shi, X. J., & Zhu, W. W. 2009, Journal of Geophysical Research (Space Physics), 114, 4101

Meunier, N. 1999, ApJ, 527, 967

Mishra, B. N., & Mishra, A. G. 2012, Indian J Phys, 86, 253

Norton, A. A., & Gallagher, J. C. 2010, Sol. Phys., 261, 193

Oliver, R., & Ballester, J. L. 1994, Sol. Phys., 152, 481

Ribes, E., & Bonnefond, F. 1990, Geophysical and Astrophysical Fluid Dynamics, 55, 241

Ribes, J. C., & Nesme-Ribes, E. 1993, A&A, 276, 549

Scherrer, P. H., et al. 1995, Sol. Phys., 162, 129

Stenflo, J. O., & Kosovichev, A. G. 2012, ApJ, 745, 129

Svalgaard, L., & Kamide, Y. 2013, ApJ, 763, 23

Sýkora, J., & Rybák, J. 2010, Sol. Phys., 261, 321

Temmer, M., Rybák, J., Bendík, P., Veronig, A., Vogler, F., Otruba, W., Pötzi, W., & Hanslmeier, A. 2006, A&A, 447, 735

Tripathi, D., Bothmer, V., & Cremades, H. 2004, A&A, 422, 337

Vizoso, G., & Ballester, J. L. 1989, Sol. Phys., 119, 411

Wang, Y.-M., Sheeley, Jr., N. R., & Nash, A. G. 1991, ApJ, 383, 431

Wenzler, T., Solanki, S. K., Krivova, N. A., & Fluri, D. M. 2004, A&A, 427, 1031

Zhang, J., Wang, Y., & Liu, Y. 2010, ApJ, 723, 1006

Zolotova, N. V., Ponyavin, D. I., Arlt, R., & Tuominen, I. 2010, Astronomische Nachrichten, 331, 765

This preprint was prepared with the AAS LaTeX macros v5.2.